Fast ionic conduction in semiconductor $CeO_{2-\delta}$ electrolyte fuel cells

Baoyuan Wang[1], Bin Zhu[1,2], Sining Yun[3], Wei Zhang[1], Chen Xia[1], Muhammad Afzal[4], Yixiao Cai[5], Yanyan Liu[4], Yi Wang[6] and Hao Wang[1]

Abstract

Producing electrolytes with high ionic conductivity has been a critical challenge in the progressive development of solid oxide fuel cells (SOFCs) for practical applications. The conventional methodology uses the ion doping method to develop electrolyte materials, e.g., samarium-doped ceria (SDC) and yttrium-stabilized zirconia (YSZ), but challenges remain. In the present work, we introduce a logical design of non-stoichiometric $CeO_{2-\delta}$ based on non-doped ceria with a focus on the surface properties of the particles. The $CeO_{2-\delta}$ reached an ionic conductivity of 0.1 S/cm and was used as the electrolyte in a fuel cell, resulting in a remarkable power output of 660 mW/cm^2 at 550 °C. Scanning transmission electron microscopy (STEM) combined with electron energy-loss spectroscopy (EELS) clearly clarified that a surface buried layer on the order of a few nanometers was composed of Ce^{3+} on ceria particles to form a $CeO_{2-\delta}@CeO_2$ core–shell heterostructure. The oxygen deficient layer on the surface provided ionic transport pathways. Simultaneously, band energy alignment is proposed to address the short circuiting issue. This work provides a simple and feasible methodology beyond common structural (bulk) doping to produce sufficient ionic conductivity. This work also demonstrates a new approach to progress from material fundamentals to an advanced low-temperature SOFC technology.

Introduction

Surface/interface structures are found to play a vital role in producing exceptional material properties. For example, topological insulators with an insulating core and electron conducting surface[1–3] displayed unique electrical conducting properties. The interface between two insulating oxides can produce superconductivity[4,5]. In addition, semiconductor/ion conductor heterointerfaces, such as $YSZ/SrTiO_3$[6,8,10] and $Ce_{0.8}Gd_{0.2}O_{2-\delta}–CoFe_2O_4$[11] composites, can enhance the ionic conductivity through two material interfaces by several orders of magnitude[6–10].

These extraordinary properties on surfaces or at interfaces indicate a new strategy to develop material functionality. Thus, a new emerging approach for oxide interfaces was established[12,13]. By tuning the electronic states, oxygen ion conducting properties can be modified at interfaces[14].

Ceria (CeO_2) has attracted extensive interest and demonstrated multifunctionality in many fields, such as catalytic applications[15–17], solar cells and photoelectrochemistry[18–20], lithium batteries[21,22], fuel cells[23–26] and a variety of other energy-related applications[25,26]. The most important characteristic of ceria is the capacity to store and release oxygen via facile Ce^{4+}/Ce^{3+} redox cycles, which largely depends on the concentration and types of oxygen vacancies in the lattice as well as surface structures and states. Unique physical properties are associated with Ce^{3+} ions and oxygen vacancies. Especially from the nanoscale perspective, non-stoichiometric oxygen atoms are present at the grain boundaries or surface, and these concomitant vacancies play an

Correspondence: Bin Zhu (zhubin@hubu.edu.cn) or Hao Wang (nanoguy@126.com) or Yi Wang (yi.cnrs@gmail.com)
[1]Hubei Key Laboratory of Ferro & Piezoelectric Materials and Devices, Faculty of Physics and Electronic Science, Hubei University, Wuhan, Hubei 430062, PR China
[2]Engineering Research Center of Nano-Geo Materials of Ministry of Education, Faculty of Materials Science and Chemistry, China University of Geosciences, 388 Lumo Road, Wuhan 430074, China
Full list of author information is available at the end of the article.

important role in determining the various chemical and physical properties of ceria. The surface state is fundamental[27,28] and demonstrates significantly different physical and chemical properties when compared to those of the bulk matrix. The role of vacancy dynamics may be very important at interfaces and on surfaces because of the high mobility and redistribution of charged vacancies[29]. Ceria can be easily reduced from CeO_2 to $CeO_{2-\delta}$ through surface reduction at low oxygen partial pressures. The changes in surface oxygen vacancies often dramatically alter material physical and electrochemical properties, especially when the ceria particle size is less than 100 nm.

It is well known that CeO_2 itself is an insulator. To improve the ionic conductivity of cerium-based oxides, aliovalent doping with rare earths and alkaline cations, such as Gd, Sm, Ca and La, introduces oxygen vacancies in the lattice as charge compensating defects and increases the ionic conductivity, where the highest level of oxide-ion conductivity was reported for Gd- and Sm-doped $Ce_{1-x}M_xO_{2-\delta}$ (M = Gd and Sm)[30,31]. Although extensive efforts have been made to utilize doped ceria as an alternative electrolyte in solid oxide fuel cells (SOFCs), several critical challenges have hindered practical application of this material as reported extensively in the literature. (i) Ceria-based electrolytes under fuel cell conditions are reduced by H_2, which can be accompanied by significant electronic conductivity to futher deteriorate the open-circuit voltage (OCV) and power output[32]. (ii) Once the ceria size is in nanometer scale, the electronic conduction is dominant; e.g., an enhancement of four orders of magnitude in the electronic conductivity was observed for CeO_2 when the particle size transitioned from the micro- to nanoscale[33]. There were two approaches published in Nature in 2000 for high ionic conduction that were based on structural doping[34] and surface mechanisms[35]. Doping to create bulk ionic conduction in a material is a central methodology in SOFC material research and development. However, alternative materials that can replace YSZ have not yet been successful; on the other hand, the surface approach has not been seriously developed in the current SOFC framework. This study highlights a new conceptual method to develop high electrical conductivity in CeO_2 without doping based on characteristic surface defects (Ce^{3+}, oxygen vacancies and superoxide radicals) combined with band energy alignment to avoid the formation of short circuits.

The CeO_2 surface approach presented in this work addresses challenges based on recent scientific understanding and results achieved on this material. In our approach, we take advantage of the ceria electronic conduction and surface defects for the successful demonstration of new advanced SOFC materials and technologies. Through simple heat treatment processes,

we created different surface defects and electrical properties to investigate the correlation between the conductivities and surface state of the CeO_2. The presence of oxygen vacancies and defects on the CeO_2 surface resulted in new electrical and band gap properties and successful SOFC application. Our study presents a new design concept for both materials and devices that will have a great impact on the next generation of advanced SOFCs.

Experimental section
Synthesis of CeO₂ powder

CeO_2 powders were prepared using the wet chemical precipitation method. In a typical synthesis procedure, 5.43 g cerium nitrate hexahydrate (Ce $(NO_3)_3 \cdot 6H_2O$) and 1.98 g ammonium bicarbonate (NH_4HCO_3) were separately dissolved in 200 ml deionized water under magnetic stirring. Then, the NH_4HCO_3 solution was used as the deposition agent and poured slowly (10 ml min^{-1}) into the Ce$(NO_3)_3 \cdot 6H_2O$ solution, which was stirred for 2 h and statically aged for 12 h at room temperature. Following filtration, the material was washed with deionized water to remove any possible ionic remnants and then a pure CeO_2 precursor was obtained. The CeO_2 precursor was dried at 120 °C for 24 h and calcined in air at 900 °C for 4 h to obtain CeO_2 powder.

Characterization

The X-ray diffraction (XRD) patterns of the as-prepared CeO_2 samples were analyzed to determine the crystallographic phases via a Bruker D8 X-ray diffractometer (XRD, Germany, Bruker Corporation) operating at 45 kV and 40 mA with Cu Kα radiation ($\lambda = 1.54060$ Å). The morphology of the samples were investigated using a JSM7100F field emission scanning electron microscope (FESEM, Japan) operating at 15 kV. To further characterize the microstructures, scanning transmission electron microscope (STEM) was performed on a JEOL ARM-200CF field emission microscope with a probe corrector and Gatan imaging filter (GIF) electron energy-loss spectrometer (EELS) operating with an accelerating voltage of 200 kV. Collection semi angle of 57.1 mrad was used to record the EELS line scan. The high angle annular dark field (HAADF) image was simulated using a multi-slice method implemented in QSTEM image simulation software. Ultraviolet photoelectron spectroscopy (UPS) measurements were performed to obtain the valence band level. The UV-vis diffused reflection spectra of the materials were tested on a UV3600 spectrometer (MIOSTECHPTY Ltd.).

Cell construction and measurement

The devices used for measurements were constructed using 0.2 g CeO_2 powder sandwiched between two thin

layers of $LiNi_{0.8}Co_{0.15}Al_{0.05}O_2$ semiconductor pasted on nickel foam and pelletized at room temperature under a hydraulic press pressure of 200 MPa to obtain a simple symmetric configuration device of (Ni)NCAL/CeO$_2$/NCAL(Ni). Two nickel foam acted as current collectors. The device was shaped as 13 mm in diameter, around 1.0 mm in thickness with an effective area of 0.64 cm^2. Pure hydrogen and ambient air were supplied to each side of the cells as fuel and oxidant, respectively. The flow rates were controlled in the range of 80–120 ml min^{-1} for H$_2$ and 150–200 ml min^{-1} for air under 1 atm. To analyze the cell performance, the voltage and current readings were collected using a programmable electronic load (IT8511, ITECH Electrical Co., Ltd.) to plot the *I–V* and *I–P* characteristics.

Electrochemical impedance spectroscopy (EIS) was carried out by using an electrochemical workstation (Gamry Reference 3000, USA) in both air and fuel cell operation atmospheres, and the frequency ranged from 0.1 Hz to 1 MHz with an amplitude of 10 mV.

Results and discussion

Figure 1 shows the XRD pattern of the CeO$_2$ powder synthesized at 900 °C for 4 h compared with that of CeO$_2$ reduced in H$_2$ at 550 °C for 1 h (R-CeO$_2$). The patterns exhibit the same fluorite structure. However, a shift towards lower angle is observed for R-CeO$_2$ sample in the expanded XRD pattern, as shown in the inset. The lattice parameters for the CeO$_2$ powder and R-CeO$_2$ calculated by Scherrer equation were 5.403 Å and 5.452 Å, respectively, suggesting a slight CeO$_2$ local lattice expansion. The XRD analysis indicates that i) the CeO$_2$ obtained at 900 °C had a normal lattice structure that agreed with the

Fig. 1 XRD patterns for CeO$_2$ treated by H$_2$ (R-CeO$_2$) at 550 °C for 1 h compared to non-H$_2$ treatment (CeO$_2$). The inset shows an enlarged view of the XRD pattern in the range of 28–32°

standard lattice parameter of 0.5410 nm indicated in the JCPDS card; and ii) the hydrogen treatment led to a reduction of Ce^{4+} to Ce^{3+}, thereby causing lattice structural changes, i.e., the lattice expanded significantly from 5.403 to 5.452 A. The large Ce^{3+} radius can bring about lattice expansion by forming non-stoichiometric CeO$_{2-\delta}$ in the CeO$_2$ fluorite structure within tolerance limitations. The effect is similar to that of large Sm^{3+} and Gd^{3+} rare earth ions doping into CeO$_2$ and cause corresponding lattice expansion.

Along with the production of Ce^{3+}, oxygen vacancies are also created in the CeO$_2$ lattice. This process can be described by:

$$2Ce^{4+} + O^{2-} \rightarrow 2Ce^{3+} + V_o^{\cdot\cdot} + 1/2O_2 \qquad (1)$$
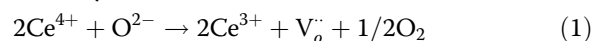
This is a fundamental way to improve CeO$_2$ electrical properties. CeO$_2$ has stoichiometry valence of Ce^{4+} which is located in the grain interior[36]. Hydrogen treatment leads to chemical defects on the CeO$_2$ particle surfaces. This process can be deemed as a surface doping process due to the replacement of Ce^{4+} by Ce^{3+}. The introduction of oxygen vacancies and accompanying large-sized Ce^{3+} ions leads to a distortion of the local symmetry and results in an increased lattice expansion, thus causing strain and surface stresses. This speculation can be directly observed in the high-resolution STEM images and is discussed in the next section. The hydrogen reduction process, e.g., during fuel cell operation or at a low oxygen partial pressure, starts from CeO$_2$ particle surfaces and approaches to the bulk, it is reasonable to consider a different surface state from the bulk to be further characterized in the following sections. The production of Ce^{3+} in CeO$_2$ can have the same effect as trivalent rare earth ions, e.g., replacing Ce^{4+} with Sm^{3+} or Gd^{3+}, that are doped in CeO$_2$ to cause CeO$_2$ a lattice expansion. We noticed that Ce^{3+} ions have an ionic radius of 1.03 Å that is larger than the value of Ce^{4+} (0.92 Å), Gd^{3+} (1.05 Å) and Sm^{3+} (1.08 Å), respectively. Therefore, producing Ce^{3+} in CeO$_2$ may result in doping effects, similar to Sm^{3+} and Gd^{3+}, and impact not only the lattice but also the ionic conductivity. However, it should be noted that Ce^{3+} is on the surface, while Sm^{3+} and Gd^{3+} are doped in the bulk[37].

We adjusted the synthesis conditions and found that the sintering temperature can play a role in determining the microstructure and electrical properties of as-prepared ceria. The detailed work with regard to sintering temperature was added in supplementary information (SI) and can be described as follows. The XRD patterns of the CeO$_2$ powder sintered at various temperatures are presented as Fig. S1 in the SI. The results can be summarized: i) different temperatures led to the same fluorite structure; ii) the CeO$_2$ crystallinity was enhanced with the sintering temperature; iii) the lattice constant decreased as the sintering temperature increased, indicating a change in
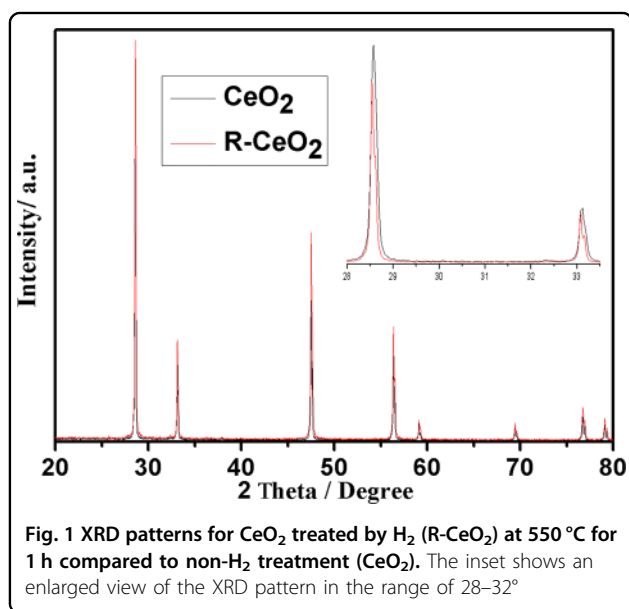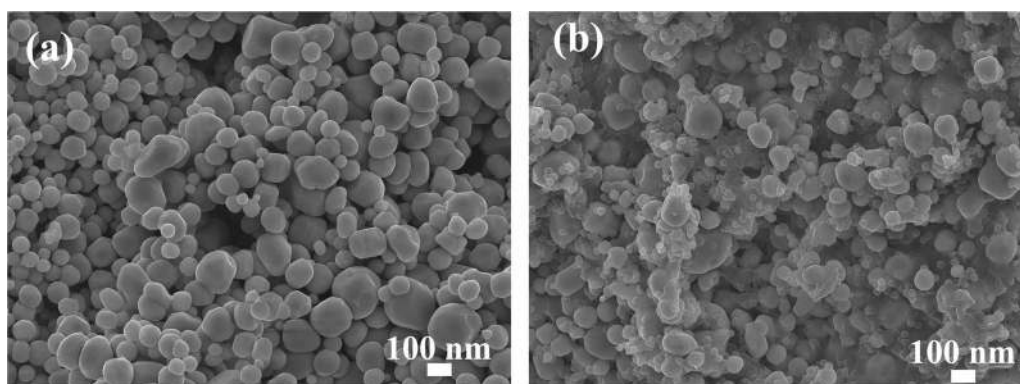
Fig. 2 SEM images of the CeO$_2$ powder (**a**) before and (**b**) after fuel cell measurements
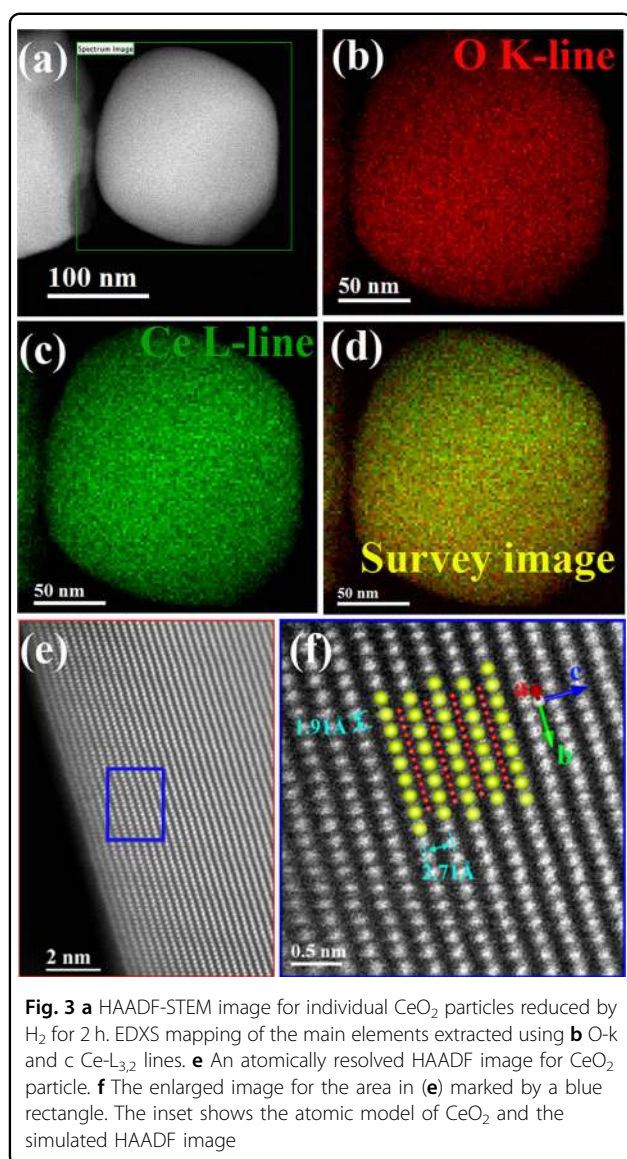
the Ce^{3+}/Ce^{4+} ratio. Upon increasing the sintering temperature from 500 to 900 °C, the lattice parameters decreased correspondingly from 5.416 to 5.403 Å, which was deduced from the XRD patterns. This may be due to Ce ions not being fully oxidized at low sintering temperature, i.e., some Ce^{3+} coexisted with Ce^{4+}. The large Ce^{3+} can expand the ceria lattice, while sintering at increased temperatures can fully oxidize the Ce ions, converting Ce^{3+} to Ce^{4+}, and lead to a normal lattice constant that agrees with standard JCDPS data. Figure S2 shows the morphology evolution of the CeO$_2$ powder with sintering temperature through SEM characterization. A clear trend is discernible indicating that the grain size increased with the sintering temperature from several nanometers (500 °C) to 200–300 nm (1000 °C), which is closely related to the electrical conductivity and activation energy of ceria. The particular sintering temperature resulted in the formation of nanoscale CeO$_2$, and the size effect possibly extended the interfacial area accompanying with a reduced enthalpy of defect formation on the CeO$_2$ crystallizes and caused a high oxygen deficiency on the ceria particle surfaces, significantly enhancing the electrochemical performance of the cells. While focusing on low-temperature (<600 °C) SOFC electrolyte applications, we carefully optimized the synthesis conditions and fixed the sintering temperature at a sufficiently high temperature of 900 °C for 4 h to address the material stability and produce excellent electrochemical performance.

Figures 2a, b display the morphological change of the CeO$_2$ particles before and after fuel cell measurements. The original CeO$_2$ particles displayed a spherical shape with a 20–200 nm size distribution, and some pores were observed in the electrolyte layer, but the pores were enclosed without penetrating through the CeO$_2$-electrolyte membrane. After the FC measurements, the gaps between the particles were filled, and the CeO$_2$ electrolyte layer presented a fair density and good gas-tightness, thus ensuring that the assembled cells possessed high OCVs

(above 1 V) and excellent power outputs (see the cell performance section below) compared with conventional cells based on a dense doped ceria electrolyte.

Figure 3a shows the HAADF-STEM image for individual CeO$_2$ particles reduced by H$_2$ for 2 h. The particle was an irregular sphere with a diameter of 190 nm. The energy dispersive X-ray spectrometer (EDXS) mapping of the main elements using O-k and Ce-L$_{3,2}$ lines for the CeO$_2$ particle is shown in Fig. 3b, c, and Fig. 3d is the survey image, which indicates an almost uniform element distribution throughout the entire particle. Figure 3e and f shows the atomically resolved HAADF-STEM image for the reduced CeO$_2$ particles. A high-resolution image is displayed in Fig. 3d, showing the atomic arrangement. An atomic structure model of the cubic phase of the CeO$_2$ along the [211] projection and a simulated HAADF image are superimposed on the HAADF image.

To further investigate the surface state of the reduced CeO$_2$ particles, the high spatial resolution of aberration-corrected STEM combined with EELS analysis were allowed to detected the valence variations of superficial Ce at the atomic scale. Figure 4a displays the particle area for EELS analysis and the blue arrow indicates the line scan direction. The plot of EELS scan signal from surface (point A) to grain interior (point B) was presented in Fiure 4b. The Ce M$_5$/M$_4$ ratio is sensitive to the chemical state of Ce; therefore, the oxidation state of Ce can be determined quantitatively from the M$_5$/M$_4$ ratio using the positive part of the second derivative of the experimental spectra. Figure 4c gives the Ce M5,4 edges extracted from particle surface and 20 nm away from the surface. The resultant intensity ratios are listed in the inserted table. It can be found that the M$_5$/M$_4$ ratio on the surface is higher than that of the interior grain. As reported, a small M$_5$/M$_4$ ratio corresponds to Ce^{4+} and a large ratio is associated with Ce^{3+}. Therefore, Ce^{3+} was produced on the surface of the CeO$_2$ particle, indicating the formation of a thin layer of oxygen-deficient CeO$_{2-\delta}$ on the surface. EELS

Fig. 3 a HAADF-STEM image for individual CeO$_2$ particles reduced by H$_2$ for 2 h. EDXS mapping of the main elements extracted using **b** O-k and c Ce-L$_{3,2}$ lines. **e** An atomically resolved HAADF image for CeO$_2$ particle. **f** The enlarged image for the area in (**e**) marked by a blue rectangle. The inset shows the atomic model of CeO$_2$ and the simulated HAADF image
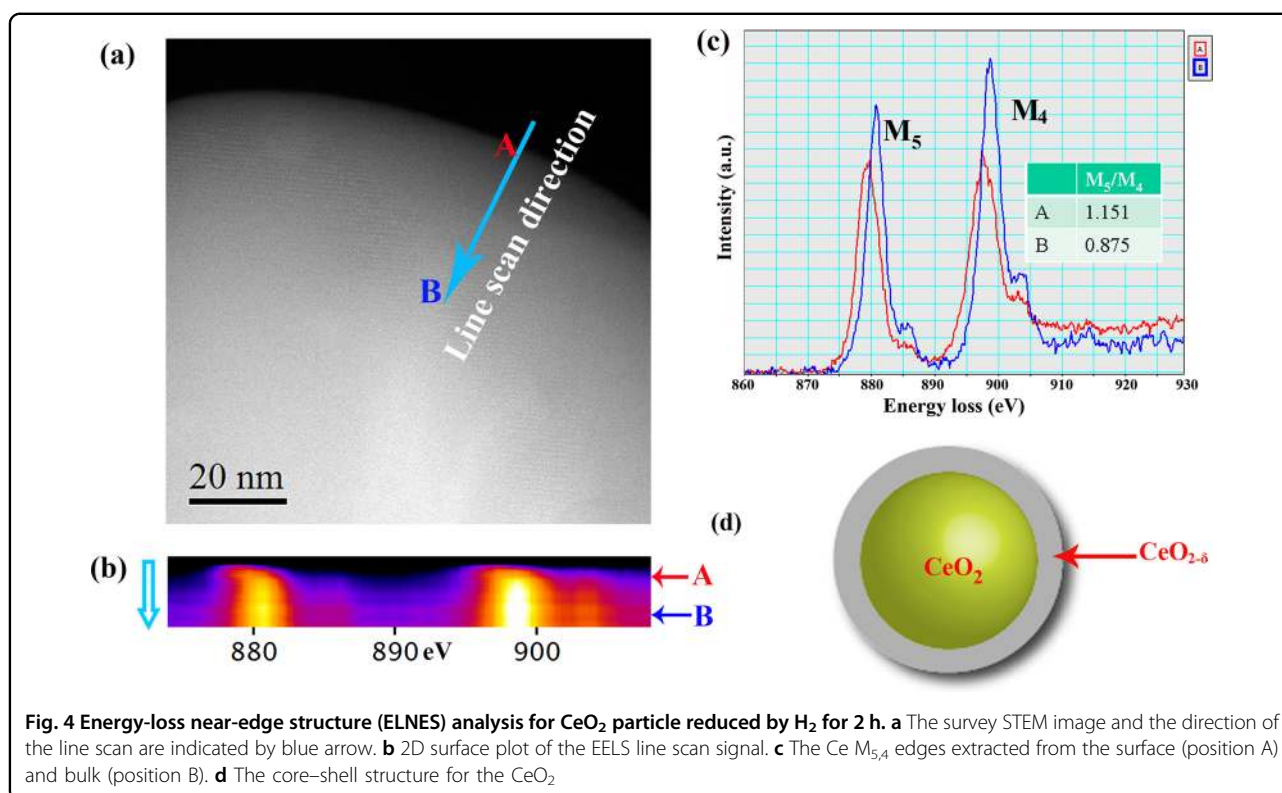
measurements confirmed the presence of oxygen vacancies on the particle surface. When a neutral oxygen vacancy is formed, two electrons are left behind. It is generally accepted that these electrons are localized in the f-state of the nearest Ce atoms[38], which changes their valence state from +4 to +3. In other words, the presence of Ce^{3+} could be evidence of oxygen vacancy formation, which significantly improves ion conductivity on the surface. Therefore, the stoichiometric CeO$_2$ in the interior grains is an insulator, and the oxygen-deficient CeO$_{2-\delta}$ on the surface possesses promising electrical conducting properties. Therefore, a novel CeO$_{2-\delta}$@CeO$_2$ structure with a topological configuration, i.e., an insulating core and high conducting shell, was formed as illustrated in Fig. 4d. This evidence clearly indicates that

there is strong ionic conductivity for the reduced CeO$_2$, which was reflected by the great power output of the fuel cells assembled from pure CeO$_2$. In fact, it was reported that a surface layer of CeO$_{1.5}$ is formed on the nano-CeO$_2$ particles, and the CeO$_{1.5}$ fraction presented a significant increase when the particle sizes were below 15 nm and reached up to 90% at 3 nm[39].

The electron core level XPS spectra of the reduced and as-prepared CeO$_2$ were obtained to peer the chemical composition and valance states of the elements. Figure 5a shows the Ce 3d spectra collected from the as-prepared CeO$_2$. The spectrum is composed of two multiplets identified as V and U. These multiplets correspond to the spin-orbit split 3d 5/2 and 3d 3/2 core holes. The u‴ and v‴ peaks with a high binding energy indicate the final state of Ce 3d^9 4f^0 O2P^6, and the peaks labeled as u, v, u″ and v″ with a low binding energy are attributed to the Ce 3d^9 4f^2 O2P^4 and Ce 3d^9 4f^1 O2P^5 final states. The six characteristic peaks can be indexed as the Ce 3d spectrum for Ce^{4+}, which is consistent with previous reports[40,41]. Besides the six characteristic peaks of Ce^{4+}, three extra peaks marked as u$_0$, u′ and v′ appeared in the Ce 3d XPS of the R-CeO$_2$ sample as Fig. 5b shown, demonstrating the existence of the Ce^{3+} oxidation state. The energy split between the v and v′ peaks is ~3.0 eV, which is close to the value observed for the Ce^{3+} compound[42]. Figure 5c, d presents the O1s XPS spectrum of the as-prepared and R-CeO$_2$, which delivered an asymmetric feature that could be deconvoluted into different symmetrical signal. The spectrum for the as-prepared CeO$_2$ sample is fitted by two peaks centered at 529.5 eV and 530.5 eV, which are attributed to the lattice oxygen (marked as O$_I$) and surface adsorbed oxygen (marked as O$_{II}$), respectively. For the R-CeO$_2$ sample, the asymmetric O1s spectrum is deconvoluted into three peaks denoted as O$_I$, O$_{II}$ and O$_{III}$. The new peak (O$_{III}$) with a higher binding energy is related to the presence of the oxygen vacancies, possibly due to the existence of Ce^{3+} produced by H$_2$ reduction, which is crucial for ionic conduction and dominated the electrochemical performance of the assembled fuel cell.

This surface layer of the core–shell structure was further characterized to understand the boundaries and buried interface effects on the ionic conduction origin and enhancement. We carried out more careful characterization to identify and determine the tension of the grain boundaries with agglomerated CeO$_{2-\delta}$ particles through STEM in combination with the EELS, as shown in Fig. 6. The HAADF images a and b show that the particle size was in the range of 10–200 nm. It is clear that all of the particles closely contacted each other, and the color of the interface region between the particles is different from the interior of the particles, indicating stress accumulation at the interface. As Fig. 6c shows, neither disordered nor amorphous structures are present at the grain boundaries,

Fig. 4 Energy-loss near-edge structure (ELNES) analysis for CeO$_2$ particle reduced by H$_2$ for 2 h. a The survey STEM image and the direction of the line scan are indicated by blue arrow. **b** 2D surface plot of the EELS line scan signal. **c** The Ce M$_{5,4}$ edges extracted from the surface (position A) and bulk (position B). **d** The core–shell structure for the CeO$_2$

indicating that the boundaries are successfully joined at the atomic level.

In Fig. 6, there are two direct pieces of evidence to support the interfacial conduction mechanism. (i) First, an analysis of the stress was carried out at the interfaces. As shown in Fig. 6a, b for the HAADF images, the contrast is bright at the interfaces, which indicates that there was an accumulation of stress. (ii) An emphasis is paid on analysis of the valency state at the interfaces. The Ce valence state changes were extracted using Ce-M$_{5,4}$ edges in atomic resolution, as shown in Fig. 6e. Both the chemical shift and white-line ratio methods and analyses prove that there was an ~1.5 nm buried interface, where Ce was in the 3 + valence state and is highlighted in red in Fig. 6d. This implies that oxygen vacancies were created in the buried interfaces. Because accompanying with the Ce^{3+} formation, the oxygen vacancy generation process can be described by equation (1). The experimental evidence indicates that the surface and grain boundaries play a dominant role in ionic transport; it is well understood and reported in the literature[43–45] that stress and tension generate vacancies at interfaces to promote ion transport.

The electrical behavior of the CeO$_2$ pellets was examined by EIS analysis under air and H$_2$/air FC environment at a device measuring temperature of 550 °C. The EIS results are shown in Fig. 7. To understand the EIS behavior in more detail, a simulation was carried out using the equivalent circuit models of R$_o$(R$_1$-QPE$_1$)(R$_2$-QPE$_2$)

(Insets of Fig. 7), where R is the resistance and QPE represents the constant phase element. The high-frequency intercept on the Z'-axis, as shown in the enlarged inset, reflects the entire ohmic resistance of the device, including the resistance of CeO$_2$ bulk, electrodes and connecting wires. Both EIS results were characterized as a semicircle followed by an inclined line, and the flat semicircle in the medium-frequency region could be superimposed by two standard semicircles. One is attributed to the grain boundary/surface effect in the middle-frequency range, and the other is due to the charge-transfer impedance on the electrode/CeO$_2$ interface. In addition, the inclined line in the low-frequency region corresponds to the ion-diffusion process in the electrode process. These processes also commonly exist in fuel cells based on doped ceria electrolytes[46]. It can be seen clearly that the CeO$_2$ based device under an air atmosphere exhibited a typical ion conducting nature and low conductivity, which are reflected by a large semicircle due to grain boundary and charge transfer processes. In the FC condition, the device immediately shows a mixed electron-ion conducting behavior and a rapid decrease in resistance of more than two orders of magnitude (see the inset of Fig. 7). The diameter of the semicircle in the medium-frequency region for the CeO$_2$ under FC conditions is much smaller than that of the CeO$_2$ device in air, indicating much lower grain boundary and charge-transfer resistances. The result suggests that the
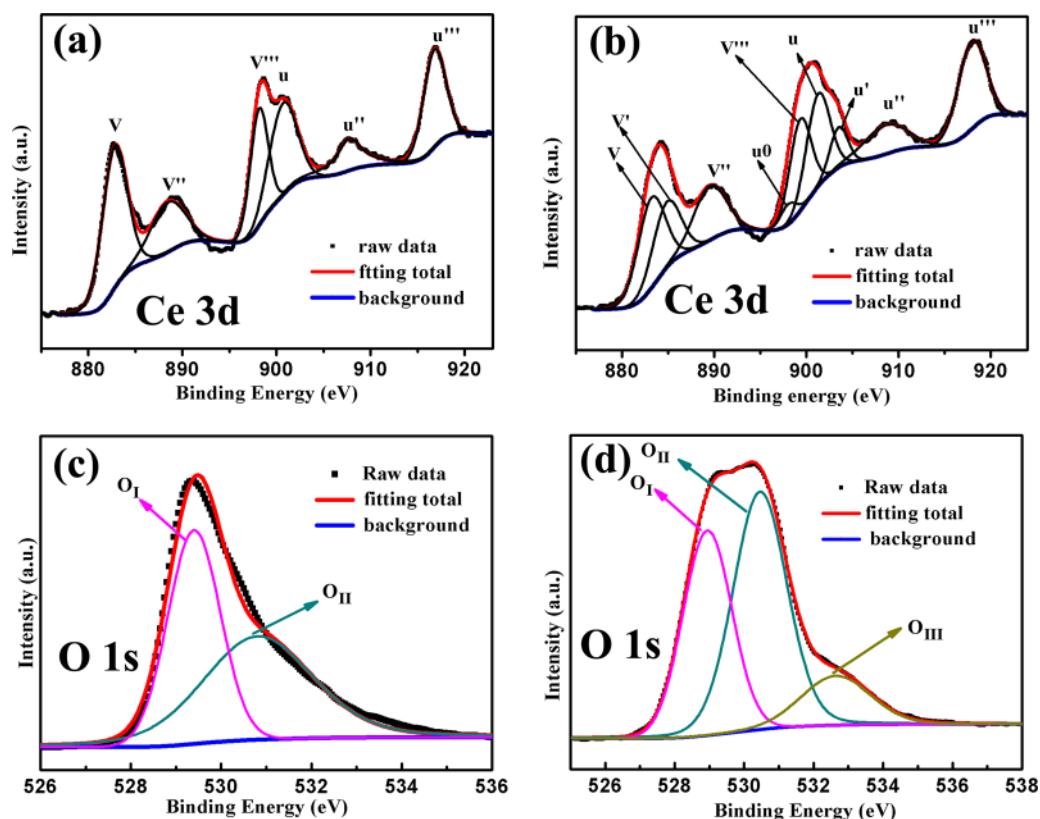
Fig. 5 Curve-fitting result for Ce 3d and O 1 s XPS spectra collected from the as-prepared **a**, **c** CeO_2 and **b**, **d** R-CeO_2

conductivity (both ions and electrons) of CeO_2 under FC conditions was significantly enhanced in comparison with that under an air atmosphere. The fitting results show that the total electrical conductivity of the CeO_2 in air was low, ~10^{-4} s/cm, as estimated from the EIS result in air; in contrast, a drastic change occurred to bring about a high conductivity state under FC conditions, and the conductivity exceeded 10^{-1} s/cm. In addition, the obtained capacitances displayed low values, revealing the rate-determining processes in the fuel cell. This result is consistent with the reduction of the Ce^{4+} to Ce^{3+} in the H_2/air environment. This occurred because H_2 can reduce CeO_2 and form large oxygen vacancies, further resulting in significant enhancement of both oxygen ion and electronic conduction.

The oxygen deficient layer on the surface can function as an oxygen ion transport pathway and significantly dominate the charge conduction, especially the grain boundary conductivity, which was deduced from the EIS plot of the pellet. To further verify the surface conduction, we specifically separated the grain boundary resistance from the EIS results and converted the resistance to conductivity by using the pellet dimensions. Figure 8 shows the grain boundary conductivity (σ_{gb}) of CeO_2 as a function of temperature obtained in air and H_2/air

atmospheres. The noteworthy point is that the σ_{gb} obtained in the H_2/air atmosphere was significantly higher than that in the air, possibly due to the formation of an oxygen-deficient layer on the particle surface under the H_2/air atmosphere, which provided a pathway for oxygen transport to significantly enhance σ_{gb}.

Based on the excellent electrical properties, the CeO_2 samples were used as the electrolytes for fuel cells, and the cell performances are shown in Fig. 9. It can be seen clearly that high OCV values (1.0 to 1.12 V) and power outputs (140–660 mW/cm^2) was achieved at operational temperatures of 400–550 °C. To verify the reproducibility of the performance, we fabricated 8 cells from non-doped CeO_2 and evaluated their electrochemical performance. A box plot diagram was chosen to present the power maximum of the measured 8 cells at various testing temperatures, as shown in Fig. 10. The horizontal lines in the box denote the 25th, 50th and 75th percentile values. Obviously, the performance presented in Fig. 9 is close to the mean value; therefore, the value is representative. Although there was high electronic conduction, as discussed above, the CeO_2 electrolyte exhibited no any electronic short-circuiting problem. These results obtained from non-doped CeO_2 surface conduction demonstrated significant advantages over doped ceria
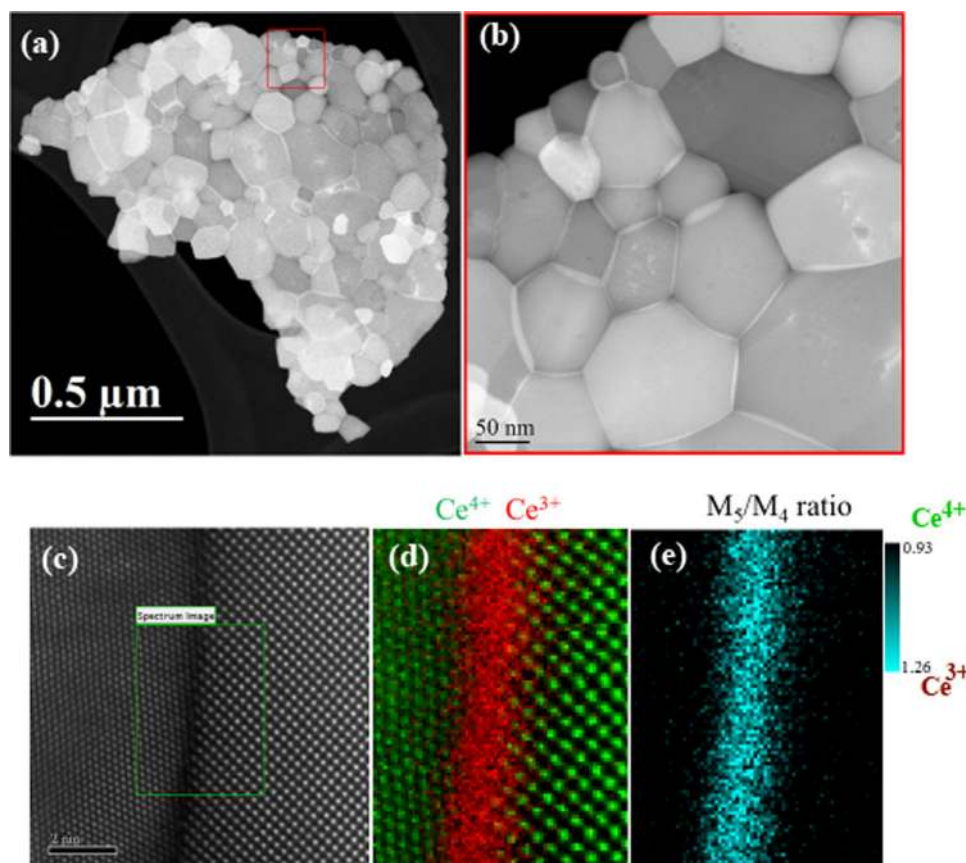
Fig. 6 a, b HAADF-STEM image for agglomerated CeO$_{2-x}$ particles. **c** The atomically resolved HAADF image for the grain boundary region, and the green rectangle marked where the EEL spectrum image was acquired. **d** Atomically resolved Ce valence state mapping obtained by multiple linear least squares fitting. **e** Ce valence state mapping deduced from Ce M$_5$/M$_4$ ratio
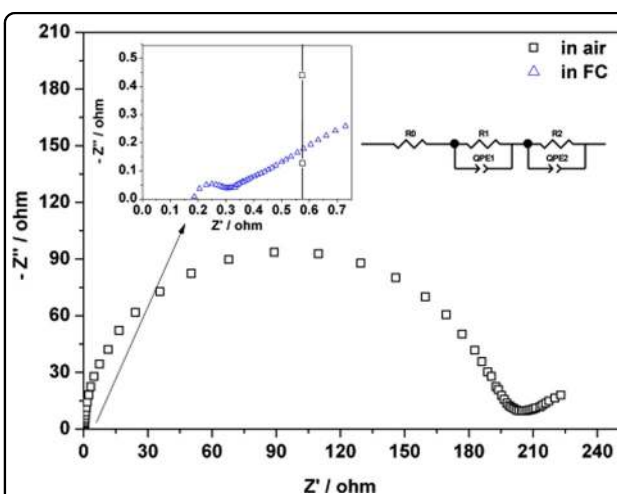

Fig. 7 EIS spectra for the CeO$_2$ devices measured in air and FC conditions

electrolyte fuel cells from both the OCV and power output perspectives. For example, samarium-doped ceria (SDC) electrolyte fuel cell devices have demonstrated OCVs < 0.9 V and output powers < 100 mW/cm^2 at 600 °C, while non-doped CeO$_2$ achieved 660 mW/cm^2 at 550 °C[32]. This indicates a very different ionic conduction mechanism and fuel cell principles between the doped bulk conducting SDC and non-doped surface conducting CeO$_2$, which deserves further study.

It has been reported that nanoscale CeO$_2$ shows strong or dominant electronic conductivity, giving nanosized CeO$_2$ a mixed ionic and electronic conductivity (MIEC) state[33]. The grain boundary-enhanced electron concentration corresponding to depression in the positively charged ionic (oxygen vacancy) species is expected from space charge theory. It should be pointed out if the fuel cell electrolyte has significant electronic conductivity, i.e., a typical MIEC electrolyte, which will make significant
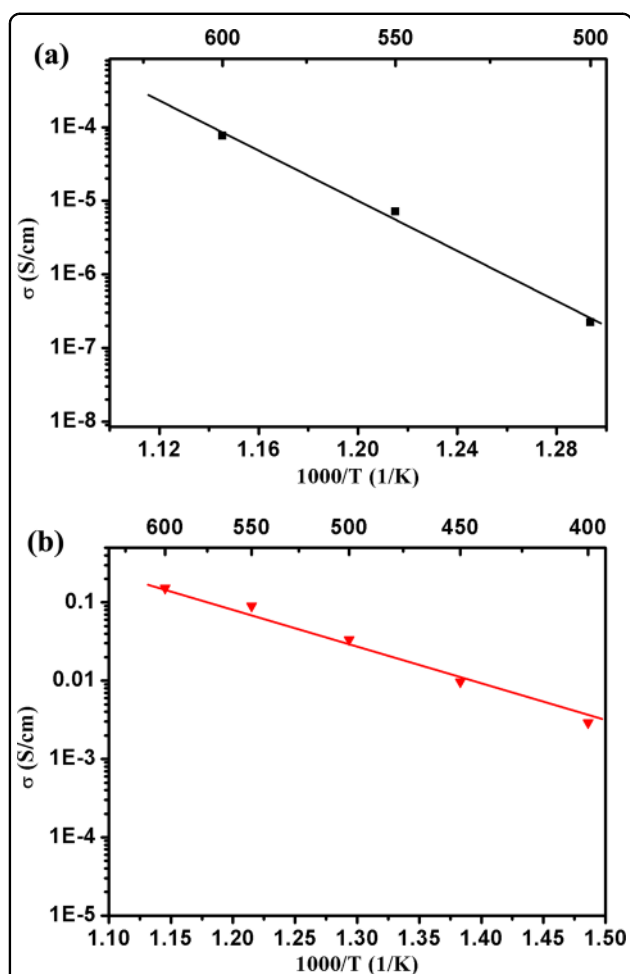
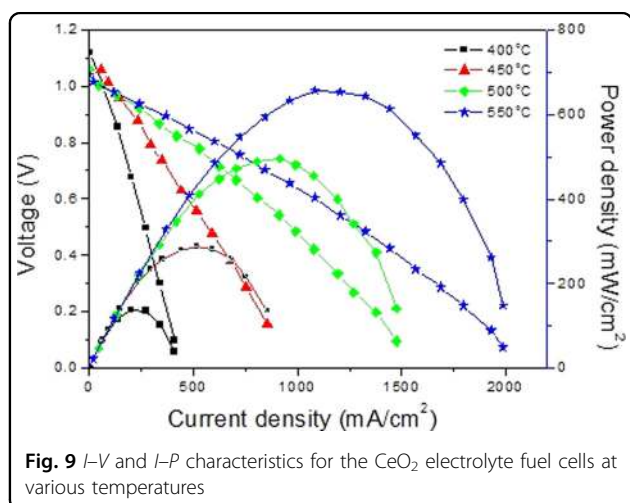**Fig. 8** The grain boundary conductivity of CeO_2 as a function of temperature obtained in (**a**) air and (**b**) H_2/air atmospheres

Fig. 9 *I–V* and *I–P* characteristics for the CeO_2 electrolyte fuel cells at various temperatures
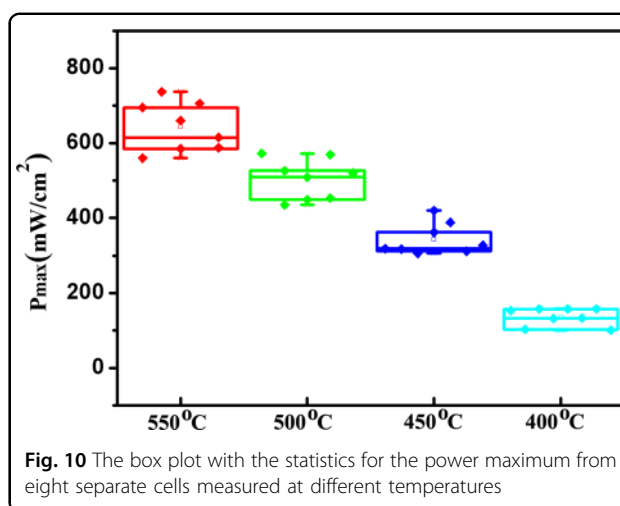
Fig. 10 The box plot with the statistics for the power maximum from eight separate cells measured at different temperatures

exceeded 1.0 V and even reached 1.12 V, and for the power output, which reached 660 mW/cm^2 at 550 °C.

How can the MIEC type CeO_2 be used as a fuel cell electrolyte and cause no additional losses in the OCV and power output? These conflict with conventional MIEC theory and SOFC devices for a doped ceria electrolyte fuel cell[33]. We propose a new scientific principle for a semiconductor junction combined with energy band alignment, which has been reported in other semiconductor-ionic membrane fuel cell systems[47,48]. In this case, the contacted CeO_2 on the anode side was reduced by H_2 to form Ce^{3+} and released free electrons. The surface conduction was formed, and the extra electrons simultaneously brought about n-type conduction for the CeO_2 on the anode side. Martin and Duprez determined the oxygen and hydrogen surface diffusion on the oxide surfaces, and pointed out that both oxygen and hydrogen can transport rapidly on the CeO_2 surface[49,50]. Lai et al. reported that a Sm-doped CeO_2 thin film exhibited mixed ionic and electronic conductivity with a bulk ionic conductivity of 7 mScm^{-1} and an electronic conductivity of 6 mScm^{-1} under open-circuit conditions at 500 °C[51]. These data agree well with our fuel cell results, although we used the pure CeO_2 phase, which possessed sufficient surface electron and ionic conductivities.

On the other hand, CeO_2 on the air side showed hole conduction[52], i.e., p-type conduction, while the CeO_2 on the anode side reduced by H_2 turns to electron (n-type) conduction. Naturally, a p-n junction was formed between two parts of the CeO_2 electrolyte. In this case, we propose a double-layer electrolyte model for the fuel cell, as shown in Fig. 11f. Band energy alignment between the CeO_2 and R-CeO_2 is proposed to clarify the charge separation and barrier to block the electron passing through the CeO_2 electrolyte, even though it is an MIEC-type electrolyte. An oxygen vacancy is associated with the formation of two Ce^{3+} ions and is a two-electron donor center, which can

device OCV and power losses. However, our case represents the opposite situation because excellent fuel cell performances were obtained for the OCV, which
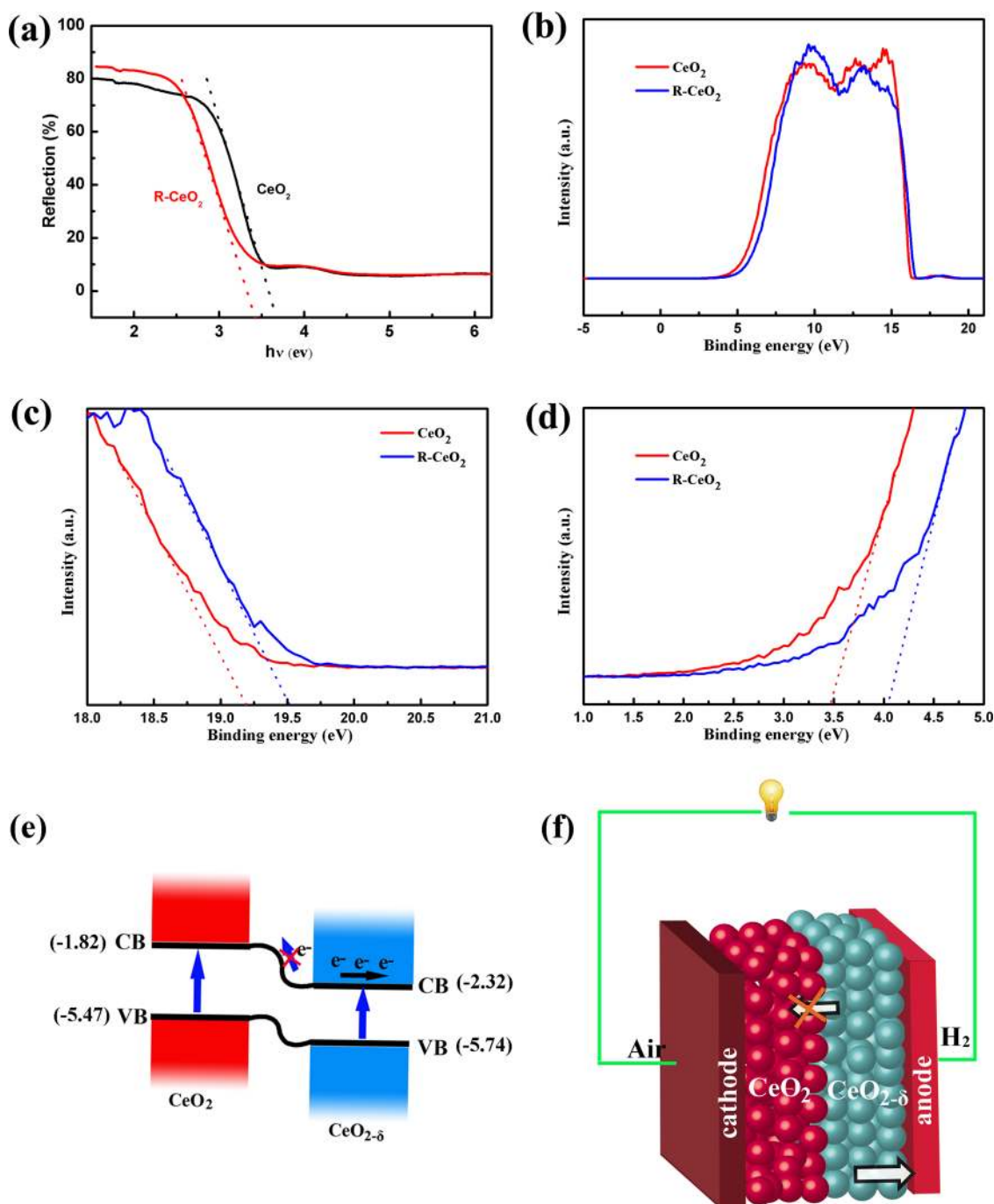
Fig. 11 a The diffused reflection spectra and **b** the UPS of as-prepared CeO$_2$ and reduced CeO$_2$. **c** UPS plots of CeO$_2$ and R-CeO$_2$ with magnified views of the low binding energy cutoff and **d** the high binding energy cutoff regions. **e** The energy alignment diagram and **f** the configuration schematic for the double-layer fuel cell using CeO$_2$ as the electrolyte

lead to significant electronic conduction. Concerning the formation of double-charged oxygen vacancies, electrons in the conduction band were composed of Ce 4 f energy states. The electrons formed during reduction were treated as being localized on the cerium, thereby converting Ce^{4+} to Ce^{3+} ions. To verify this assumption, the accurate

band energy of the CeO$_2$/R-CeO$_2$ was determined by UPS combined with UV-vis diffused reflection. UPS of the CeO$_2$ and R-CeO$_2$ were carried out to determine their valence band. In the UPS spectra presented in Fig. 11b, the energy was calibrated with respect to He I photon energy (21.21 eV). As Fig. 11c, d shows, by defining the

low-binding and high-energy cutoff, the valence band maximum below vacuum level was obtained to be -5.47 eV for CeO_2 and -5.74 eV for the R-CeO_2 sample. These band gaps were determined from the diffused reflection measurements (Fig. 11a) to be 3. 65 eV and 3.42 eV for CeO_2 and R-CeO_2, respectively. On the basis of these results, we can further deduce the corresponding conduction band (CB) levels to be 1.85 eV for CeO_2 and 2.32 eV for R-CeO_2. The final band alignment is sketched in Fig. 11e and clearly reveals that the CB position of CeO_2 is higher than that of R-CeO_2, the extra electrons produced by the reduction atmosphere should aggregate in the CB of the R-CeO_2, further decreasing the CB position. The conduction band offset formed potential barriers to prevent the electrons generated on the anode side from passing through the interface between CeO_2 and R-CeO_2, thus avoiding a short-circuiting problem. In addition, the built-in field formed by the CeO_2/R-CeO_2 band energy alignment should promote oxygen ion transport.

In the present work, we discovered that CeO_2 without doping can create much better electrical properties and fuel cell performance than those of conventional cation doped ceria, e.g., samarium-doped ceria (SDC) based on bulk ionic conduction. The possible underlying mechanism involves the formation of a surface oxygen-deficient layer and core–shell architecture for reduced CeO_2 that is accompanied by band energy alignment to avoid shorting, which is a novel mechanism for ceria electrolyte materials and a novel fuel cell principle. On the other hand, the H_2 supplied as fuel reduces the Ce^{4+} into Ce^{3+}, which has the same doping effect as Sm^{3+} and improves the ionic conductivity, namely, "self-doping" occurs. However, cation doping and self-doping are different. For example, cation doping, such as with Sm^{3+} or Gd^{3+} takes place in the CeO_2 particle bulk to create oxygen vacancies, further developing bulk conduction, while self-doping occurs at the particle surface accompanied by oxygen vacancies, leading to different surface conduction mechanisms. Surface conduction has unique advantages, including low activation energy and fast ionic mobility. Both of these advantages contribute to better ionic conductivity and fuel cell performance than conventional cation doped cerium-based electrolytes. For example, Shen et al. reported a Gd-doped ceria (GDC) electrolyte for SOFCs with mixed electronic conduction, resulting in an OCV < 0.9 V and power output < 100 mW/cm[32]. In other words, the surface conduction induced by fuel cell conditions is distinct from the ordinary O^{2-} conduction mechanism in bulk doped ceria and appears to be a new methodology for the design of new functionalities for advanced technologies in the energy sector, especially for next generation SOFCs.

Conclusions

The occurrence of charged defects and the control of stoichiometry in fluorite CeO_2 materials can be accomplished by a reduction treatment, which can strongly affect the CeO_2 surface defects. Reducing and oxidizing conditions during cell operation produce CeO_2 semi-conducting (n-type at the anode and p-type at the cathode)-ionic properties and greatly enhance both the electronic and ionic conductivities. Ionic conductivity may play a dominant role in fuel cell processes and device performance accompanied by sufficient electron conduction. High ionic conductivities have been realized by creating surface defects, e.g., oxygen vacancies and surface pathways. The CeO_2 should be reduced to non-stoichiometric $CeO_{2-\delta}$ at the anode region and combined with CeO_2 at the cathode side to form a double-layer device. The energy band alignment between $CeO_{2-\delta}$/CeO_2 can produce efficient charge separation and avoid the device short circuiting problem, while charge separation is an enormous challenge for conventional SOFCs based on a doped ceria electrolyte, where OCV and power losses generally occur to some extent due to the existence of electronic conduction. The semi-conducting and ionic properties take advantage of the semiconductor energy band to prevent the electrons from internally migrated simultaneously enhance the ionic transport. The synergistic effect to enhance the ionic conductivity is also observed above 0.1 S/cm at 550 °C. The non-doped CeO_2 approach may instigate very interesting new fundamental understanding of the science and promote SOFC development.

Author details
[1]Hubei Key Laboratory of Ferro & Piezoelectric Materials and Devices, Faculty of Physics and Electronic Science, Hubei University, Wuhan, Hubei 430062, PR China. [2]Engineering Research Center of Nano-Geo Materials of Ministry of Education, Faculty of Materials Science and Chemistry, China University of Geosciences, 388 Lumo Road, Wuhan 430074, China. [3]Functional Materials Laboratory (FML), School of Materials & Mineral Resources, Xi'an University of Architecture and Technology, Xi'an 710055, China. [4]Department of Energy Technology, KTH Royal Institute of Technology, Stockholm SE-10044, Sweden. [5]State Key Laboratory for Modification of Chemical Fibers and Polymer Materials, Textile Pollution Controlling Engineering Centre of Ministry of Environmental Protection, College of Environmental Science and Engineering, Donghua University, 2999 Ren'min North Road, Shanghai 201620, China. [6]Max Planck Institute for Solid State Research, Heisenbergstr. 1, 70569 Stuttgart, Germany

Conflict of interest
The authors declare that they have no conflict of interest.

References

1. Moore, J. E. The birth of topological insulators. *Nature* **464**, 194–198 (2010).
2. Cava, R. J., Ji, H. W., Fuccillo, M. K., Gibson, Q. D. & Hor, Y. S. Crystal structure and chemistry of topological insulators. *J. Mater. Chem. C.* **1**, 3176–3189 (2013).
3. Roche, F. O. S., Valenzuela, O. & Topological, S. *Insulators Fundamentals and Perspectives.* (Wiley, Hoboken, 2015).
4. Reyren, N. et al. Superconducting Interfaces Between Insulating Oxides. *Science* **317**, 1196–1199 (2007).
5. Ben Shalom, M., Sachs, M., Rakhmilevitch, D., Palevski, A. & Dagan, Y. Tuning spin-orbit coupling and superconductivity at the SrTiO$_3$/LaAlO$_3$ interface: a magnetotransport study. *Phys. Rev. Lett.* **104**, 126802 (2010).
6. Garcia-Barriocanal, J. et al. Colossal ionic conductivity at interfaces of epitaxial ZrO$_2$:Y$_2$O$_3$/SrTiO$_3$ heterostructures. *Science* **321**, 676–680 (2008).
7. Kilner, J. A. Ionic conductors: feel the strain. *Nat. Mater.* **7**, 838–839 (2008).
8. Lee, S. et al. Ionic conductivity increased by two orders of magnitude in micrometer-thick vertical yttria-stabilized ZrO$_2$ nanocomposite films. *Nano Lett.* **15**, 7362–7369 (2015).
9. Yang, S. M. et al. Strongly enhanced oxygen ion transport through samarium-doped CeO$_2$ nanopillars in nanocomposite films. *Nat. Commun.* **6**, 8588 (2015).
10. O'Sullivan, M. et al. Interface control by chemical and dimensional matching in an oxide heterostructure. *Nat. Chem.* **8**, 347–353 (2016).
11. Lin, Y., Fang, S., Su, D., Brinkman, K. S. & Chen, F. Enhancing grain boundary ionic conductivity in mixed ionic–electronic conductors. *Nat. Commun.* **6**, 6824 (2015).
12. Hwang, H. Y. et al. Emergent phenomena at oxide interfaces. *Nat. Mater.* **11**, 103–113 (2012).
13. Mannhart, J. & Schlom, D. G. Oxide interfaces—an opportunity for electronics. *Science* **327**, 1607–1611 (2010).
14. Leon, C., Santamaria, J. & A.Boukamp, B. Oxide interfaces with enhanced ion conductivity. *MRS Bull.* **38**, 1056–1063 (2013).
15. Fu, Q., Saltsburg, H. & Flytzani-Stephanopoulos, M. Active nonmetallic Au and Pt species on ceria-based water-gas shift catalysts. *Science* **301**, 935–983 (2003).
16. Deluga, G. A., Salge, J. R., Schmidt, L. D. & Verykios, X. E. Renewable hydrogen from ethanol by autothermal reforming. *Science* **303**, 993–997 (2004).
17. Alessandro, T., Carla, de, L., Marta, B. & Giuliano, D. The utilization of ceria in industrial catalysis. *Catal. Today* **50**, 353–367 (1999).
18. Cormai, A., Atienzari, P., Garciai, H. & Chane-Ching, J.-Y. Hierarchically mesostructured doped CeO$_2$ with potential for solar-cell use. *Nat. Mater.* **3**, 394–397 (2004).
19. Carvalho, L. G. A. et al. Color tunability in green, red and infra-red upconversion emission in Tm^{3+}/Yb^{3+}/Ho^{3+} co-doped CeO$_2$ with potential application for improvement of efficiency in solar cells. *J. Lumin.* **159**, 223–228 (2015).
20. Lu, X. H. et al. Facile synthesis of free-standing CeO$_2$ nanorods for photo-electrochemical applications. *Chem. Commun.* **46**, 7721–7723 (2010).
21. Hua, C. X. et al. Q. Lithium storage mechanism and catalytic behavior of CeO$_2$. *Electrochem. Commun.* **25**, 66–69 (2012).
22. Wang, G., Bai, J. T., Wang, Y. H., Ren, Z. Y. & Bai, J. B. Prepartion and electrochemical performance of a cerium oxide–graphene nanocomposite as the anode material of a lithium ion battery. *Scr. Mater.* **65**, 339–342 (2011).
23. Steele, B. C. H. & Heinzel, A. Materials for fuel-cell technologies. *Nature* **414**, 345–352 (2001).
24. Park, S. D., Vohs, J. M. & Gorte, R. J. Direct oxidation of hydrocarbons in a solid-oxide fuel cell. *Nature* **404**, 265–267 (2000).
25. Melchionna, M. & Fornasiero, P. The role of ceria-based nanostructured materials in energy applications. *Mater. Today* **17**, 349–357 (2014).
26. Sun, C. W., Li, H. & Chen, L. Q. Nanostructured ceria-based materials: synthesis, properties, and applications. *Energy Environ. Sci.* **5**, 8475–8505 (2012).
27. Campbell, C. T. & Peden, C. H. F. Oxygen vacancies and catalysis on ceria surfaces. *Science* **309**, 713–714 (2005).
28. Knoblauch, N., Dörrer, L., Fielitz, P., Schmücker, M. & Borchardt, G. Surface controlled reduction kinetics of nominally undoped polycrystalline CeO$_2$. *Phys. Chem. Chem. Phys.* **17**, 5849–5860 (2015).
29. Chen, X. Y., Yu, J. S. & Adler, S. B. Thermal and chemical expansion of Sr-doped lanthanum cobalt oxide (La$_{1−x}$Sr$_x$CoO$_{3−\delta}$). *Chem. Mater.* **17**, 4537–4546 (2005).
30. Hong, T., Zhang, Y. X. & Brinkman, K. Enhanced oxygen electrocatalysis in heterostructured ceria electrolytes for intermediate-temperature solid oxide fuel cells. *ACS Omega* **3**, 13559–13566 (2018).
31. Zhang, T. S., Peter, H., Huang, H. T. & Kilner, J. Ionic conductivity in the CeO$_2$–Gd$_2$O$_3$ system (0.05≤Gd/Ce≤0.4) prepared by oxalate coprecipitation. *Solid State Ion.* **148**, 567–573 (2002).
32. Shen, S. L., Yang, Y. P., Guo, L. J. & Liu, H. T. A polarization model for a solid oxide fuel cell with a mixed ionic and electronic conductor as electrolyte. *J. Power Sources* **256**, 43–51 (2014).
33. Tschöpe, A. & Birringer, R. Grain size dependence of electrical conductivity in polycrystalline cerium oxide. *J. Electroceram.* **7**, 169–177 (2001).
34. Goodenough, J. B. Oxide-ion conductors by design. *Nature* **404**, 821–823 (2000).
35. Chadwick, A. V. Solid progress in ion conduction. *Nature* **408**, 925–926 (2000).
36. Feng, B. et al. Atomic structures and oxygen dynamics of CeO$_2$ grain boundaries. *Sci. Rep.* **6**, 20288 (2015).
37. Fu, Y.-P., Chen, S.-H. & Huang, J.-J. Preparation and characterization of Ce$_{0.8}$M$_{0.2}$O$_{2−\delta}$ (M = Y, Gd, Sm, Nd, La) solid electrolyte materials for solid oxide fuel cells. *Int. J. Hydrog. Energy* **35**, 745–752 (2010).
38. Skorodumova, N. V., Simak, S. I., Lundqvist, B. I., Abrikosov, I. A. & Johansson, B. Quantum origin of the oxygen storage capability of ceria. *Phys. Rev. Lett.* **89**, 166601 (2002).
39. Wu, L. J. et al. Oxidation state and lattice expansion of CeO$_{2−x}$ nanoparticles as a function of particle size. *Phys. Rev. B* **69**, 125415 (2004).
40. Ho, C. M. et al. Morphology-controllable synthesis of mesoporous CeO$_2$ nano- and microstructures. *Chem. Mater.* **17**, 4514–4522 (2005).
41. Zhou, Y. H., M. Perket, J. & Zhou, J. Growth of Pt nanoparticles on reducible CeO$_2$ (111) thin films: effect of nanostructures and redox properties of ceria. *J. Phys. Chem. C.* **114**, 11853–11860 (2010).
42. Bêche, E. et al. Ce 3d XPS investigation of cerium oxides and mixed cerium oxide (Ce$_x$Ti$_y$Oz). *Surf. Interface Anal.* **40**, 264–267 (2008).
43. Gázquez, J. et al. Applications of STEM-EELS to complex oxides. *Mat. Sci. Semicon. Proc.* **65**, 49–63 (2017).
44. Hojo, H. et al. Atomic structure of a CeO$_2$ grain boundary: the role of oxygen vacancies. *Nano Lett.* **10**, 4668–4672 (2010).
45. Song, K. P. et al. Cerium reduction at the interface between ceria and yttria-stabilised zirconia and implications for interfacial oxygen non-stoichiometry. *APL Mater.* **2**, 032104 (2014).
46. Yan, D. T. et al. Electrical properties of grain boundaries and size effects in samarium-doped ceria. *J. Power Sources* **195**, 6486–6490 (2010).
47. Zhu, B. et al. Novel fuel cell with nanocomposite functional layer designed by perovskite solar cell principle. *Nano Energy* **19**, 156–164 (2016).
48. Zhu, B. et al. Charge separation and transport in La$_{0.6}$Sr$_{0.4}$Co$_{0.2}$Fe$_{0.8}$O$_{3-\delta}$ and ion-doping ceria heterostructure material for new generation fuel cell. *Nano Energy* **37**, 195–202 (2017).
49. Martin, D. & Duprez, D. Mobility of surface species on oxides. 1. Isotopic Exchange of 18O$_2$ with 16O of SiO$_2$, Al$_2$O$_3$, ZrO$_2$, MgO, CeO$_2$, and CeO$_2$-Al$_2$O$_3$. Activation by noble metals. Correlation with oxide basicity. *J. Phys. Chem. C.* **100**, 9429–9438 (1996).
50. Martin, D. & Duprez, D. Mobility of surface species on oxides. 2. Isotopic exchange of D$_2$ with H of SiO$_2$, Al$_2$O$_3$, ZrO$_2$, MgO, and CeO$_2$: Activation by rhodium and effect of chlorine. *J. Phys. Chem. B* **101**, 4428–4436 (1997).
51. Lai, W. & Haile, S. M. Impedance spectroscopy as a tool for chemical and electrochemical analysis of mixed conductors: a case study of ceria. *J. Am. Ceram. Soc.* **88**, 2979–2997 (2005).
52. Yokokawa et al. Thermodynamic reconsiderations on electronic properties of pure- and doped-ceria. *ECS Trans.* **28**, 165–172 (2010).